#27
4/28/80
346 NTIS

UCID- 18602

FINITE ELEMENT SIMULATIONS OF THERMALLY INDUCED CONVECTION IN AN ENCLOSED CAVITY

C. D. Upson
P. M. Gresho
R. L. Lee

MASTER

March 1980

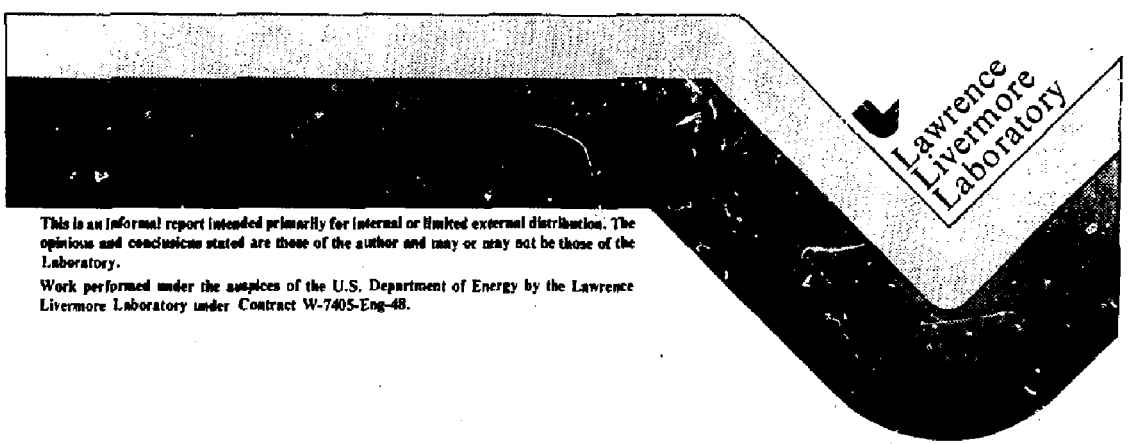

Part 1

THE BASIC BENCHMARK SIMULATIONS

Problem Specifications

The problem of interest is a two dimensional unit square cavity containing a viscous fluid ($u = w = 0$ on all boundaries). The two vertical walls are kept at uniform temperatures differing by a constant amount, ΔT, the left being hotter. The horizontal faces are fully insulated ($\partial T/\partial z = 0$), and gravity is acting in the negative z direction. The Prandtl number is kept constant at .71, and the Rayleigh number assumes the values: 10^3, 10^4, 10^5, and 10^6.

Governing Equations and Computational Method

The hydrodynamic flows of interest here are governed by the incompressible Navier-Stokes equations incorporating the Boussinesq approximation coupled with the thermal convection-diffusion equation. The time independent equations of motion and continuity for a constant property Newtonian fluid are:

$$\underline{u} \cdot \nabla \underline{u} = \nabla \cdot \underline{\underline{\tau}} + \gamma \rho g \underline{k} T \qquad (1)$$

$$\nabla \cdot \underline{u} = 0 \qquad (2)$$

Where $\underline{u} = (u,w)$ is the velocity in the x and z dimensions respectively, ρ is the constant density at reference temperature, γ is the coefficient of thermal expansion, g is the acceleration due to gravity, $\underline{k}$ is a unit vector $(\sin\theta, \cos\theta)$, θ being the angle between the negative z axis and the gravitational force vector and is positive in the clockwise direction.

T is the deviation from reference temperature, and $\underline{\tau}$, the symmetric stress tensor, is defined by:

$$\tau_{ij} = - P\delta_{ij} + \mu\left(\frac{\partial u_i}{\partial x_j} + \frac{\partial u_j}{\partial x_i}\right) \quad . \tag{3}$$

P is the pressure deviation from hydrostatic, δ_{ij} is the Kronecker delta function, and μ is the constant bulk viscosity. The energy equation is

$$\underline{u} \cdot \nabla T = \kappa \nabla^2 T \tag{4}$$

where κ is the coefficient of thermal diffusivity. Employing the suggested nondimensionalization[2] leads to:

$$\underline{u} \cdot \nabla \underline{u} = -\nabla P + Pr[\nabla^2 \underline{u} + \nabla(\nabla \cdot \underline{u})] + (PrRa)T\,\underline{k} \tag{5}$$

$$\nabla \cdot \underline{u} = 0 \tag{6}$$

$$\underline{u} \cdot \nabla T = \nabla^2 T \tag{7}$$

Here Pr is the Prandtl number:

$$Pr = \frac{\mu}{\rho\kappa} \tag{8}$$

and Ra is the Rayleigh number:

$$Ra = \frac{\rho\gamma g\, \Delta T\, D^3}{\mu\kappa} \tag{9}$$

where D is the characteristic length scale (distance between hot and cold surfaces).

Eqns. 5-7 will be solved via the penalty method[3] using finite elements. We believe that this approach, in conjunction with the quadratic (9-node) element, is "optimal" in yielding an exceptionally accurate as well as efficient solution. The penalty formulation can be

interpreted as a technique which employs, in place of Eqn. 6, a pseudo "equation of state":

$$P = -\lambda \nabla \cdot \underline{u} \tag{10}$$

where λ is a "penalty parameter" of large enough magnitude to assure (since P is finite) that the continuity equation has been closely satisfied (to $O(1/\lambda)$). This results in a very slightly compressible fluid with λ taking on the analogy of the bulk modulus.[3] For contained flows, the arbitrary pressure constant is automatically determined by

$$\int_{\Omega} P dA = 0, \tag{11}$$

which is obtained by integrating Eqn. 10 over the domain (Ω). Substituting Eqn. 10 into Eqn. 5 leads to

$$\underline{u} \cdot \nabla \underline{u} = (Pr + \lambda) \nabla(\nabla \cdot \underline{u}) + Pr\, \nabla^2 \underline{u} + (PrRa)\, T\, \underline{k} \tag{12}$$

and thus the continuity equation has been eliminated along with explicit reference to the pressure. In this formulation the constraints on λ for an accurate solution are:

$$\lambda >> Ra$$

to insure incompressibility, and

$$\lambda \leq \sim 10^8$$

to avoid significant rounding errors (CDC-7600 computer) which restricts the primary flow parameter Ra to be less than 10^6-10^7.

The roundoff-induced lower bound on Ra can be eased by employing the following nondimensionalized form of the governing equations:

$$\sqrt{\frac{Ra}{Pr}}\, \underline{u} \cdot \nabla \underline{u} = (1 + \lambda) \nabla(\nabla \cdot \underline{u}) + \nabla^2 \underline{u} + \sqrt{\frac{Ra}{Pr}}\, T\, \underline{k} \tag{13}$$

$$\sqrt{PrRa}\ \underline{u} \cdot \nabla T = \nabla^2 T \tag{14}$$

This nondimensionalization (in which the characteristic velocity is $\sqrt{\gamma g D \Delta T}$ rather than κ/D) has been employed for two reasons: first it results in dimensionless velocities and pressures that are of order unity, and secondly, it allows simulation at larger Ra since the penalty method is more accurate in this form; the lower bound on λ is now $\lambda >> \sqrt{Ra/Pr}$, which permits high accuracy at much larger Ra numbers. All data reported in this paper have been converted to be consistent with Eqns. 7&12, although we use Eqn. 13&14 in our calculations.

The solution of Eqns. 13 and 14 has been numerically approximated using the finite element method in a Galerkin formulation.[3] In these simulations we have used biquadratic approximations for $\underline{u}$ and T with bilinear discontinuous approximations for P (the pressure nodes are located at the 2 by 2 Gauss points of each 9 node element, effected by using reduced (2x2) integration on the penalty term in Eqn. (13); see 3). The resultant nonlinear equations were solved using Newton-Raphson iteration on the coupled ($\underline{u}$, T) system, with a relative combined RMS error norm of 10^{-4} defining convergence. The concomitant linear algebraic systems were solved using a disk-based unsymmetric frontal elimination method[4] without pivoting. The solution at a lower Ra was (usually) used as an initial guess for the next higher computation.

The local and average heat fluxes have each been calculated two ways. In the first two simulations (Ra = 10^3, 10^4), no significant heat flux difference could be noticed; for Ra = 10^5 the two methods differ slightly, mainly in the location of the maximum heat flux, or maximum Nusselt number (Nu). At Ra = 10^6 and (especially) 10^7, the differences become pronounced.

The first, more conventional method is simply computing the outward normal derivative of temperature at the vertical walls, utilizing the

interpolation functions in the element. These values are computed and reported at the two Gauss points on the boundary of each element and hence this technique will be referred to as the "Gauss point method" (gp) in the text and illustrations.

The second mode of Nusselt number calculation is based on global conservation of energy, and is referred to as the "consistent flux method", (cf). For this particular problem, the symmetry of the solutions results in global heat balances for both methods; however, in general only the cf method can achieve this result. The new technique of heat flux calculation, inspired by Marshall et al.,[3] which includes terms for convective as well as conductive heat transport, is given by

$$q_i \int_\Gamma \phi_i = - \int_\Omega (\phi_i \, \underline{u} \cdot \nabla T + \nabla \phi_i \cdot \nabla T) \quad , \tag{15}$$

where Γ is the portion of the boundary on which the temperature was specified, q_i is the consistent heat flux at the i-th node on Γ ($q_i \int_\Gamma \phi_i = - \int_\Gamma \phi_i \, \underline{n} \cdot \nabla T$), and ϕ_i the biquadratic basis function associated with this node. For further details on this method, in this and other contexts, see reference 5.

Numerical Results

The computational domain (Fig. 1a) consists of 168 isoparametric elements (745 nodes). The discretization chosen has larger elements in the central area (ΔX_{max} = .0845) and is graded toward smaller elements near the walls (ΔX_{min} = .0175); in addition the corners have been further refined (Fig. 1b) in order to better resolve the flow complexities expected at large Rayleigh number (ΔX_{min} in the corners is .0044). In the penalty formulation, this grid results in a system of

2235 equations which, on a CDC-7600, required 24 seconds per iteration (with a 78000 word in-core storage requirement) and an average of 5 iterations per simulation. The 672 pressures, obtained via Eqn. 10 in a post-processing manner, are computed at the Gauss points; however for display purposes, the resulting pressure field is "smoothed" to the nodes via scheme 4 in reference 6 (pressures at element corners are obtained by linear extrapolation from the 2 x 2 Gauss points with the results then averaged over all contributing elements at each corner node).

The results of the basic simulations are presented in Figures 2-11 and Table 2, but first we digress briefly to show the sensitivity of the results to the value of the penalty parameter λ. In Table 1 is shown the calculated stream function, ψ, for Ra = 10^6 at the center of the cavity (in some sense a measure of flow strength) for several values of λ, showing the desired insensitivity for $\lambda \geq 10^6$. We used $\lambda = 10^8$ for all other simulations reported herein.

TABLE 1.

λ	10^2	10^3	10^4	10^5	10^6	10^7	10^8	10^9
$\psi_{(.5,.5)}$	15.981	16.866	16.424	16.372	16.366	16.366	16.366	16.366

For Ra = 10^3 and 10^4 the velocity fields are highly symmetric (Fig. 2a,b, 5a,b) and quite similar. In both cases no sharp boundary layer can be determined and the flow fills the cavity. The simulation at Ra = 10^4 shows the onset of a behavior characteristic of higher

Rayleigh number flow; i.e., the development of a stratified central core region (see also Fig. 3b). At Ra = 10^5 three major changes can be seen: (1) the development of secondary recirculation eddies (Fig. 2c), (2) the substantial horizontal temperature gradient near the walls (Fig. 9c), and (3) the lower left and upper right corners have become much more active than the other two (Fig. 5c).

The new basic flow pattern is now established and as the Rayleigh number increases to 10^6 no major changes are observed. Notable in this flow is the vortex intensification (with the possible emergence of a tertiary recirculation with counterclockwise rotation in the core), the thinning of the vertical boundary layers, the further migration of the secondary vortex centers towards the walls, and the hydrostatically dominated pressure field (Fig. 4d; $P \sim \int T dz$).

An overall summary of selected results is contained in Table 2 (for higher accuracy, velocity and consistent flux Nusselt number extrema have been interpolated using the basis functions and are thus generally not coincident with nodal points).

Gill[7] predicts the major boundary layer characteristics of high Rayleigh number flow quite well. In his analysis the boundary layer thickness, ℓ, is estimated by an appropriate balance of terms, as

$$\ell/D \approx Re^{-1/4} \qquad (16)$$

Thus for Ra = 10^6 a boundary thickness of 0.0316 is predicted and 0.0178 for Ra = 10^7. The node closest to the boundary in the computational domain used here is located at x = 0.0175, and hence the grid probably isn't fine enough to sufficiently resolve the fluid motion

and thermal characteristics of this more difficult ($Ra = 10^7$) flow. When the scaled vertical velocity ($w/\sqrt{Ra}$) is plotted versus an expanded horizontal length scale ($x \sqrt[4]{Ra}$), the excellent correlation for high Rayleigh number flow can be seen (Fig. 11a). Readily apparent also is the theory's "failure" below $Ra = 10^5$. Gill's assumption relies on a boundary layer thickness, ℓ, which is small compared to the overall horizontal length scale D; a valid upper bound of this ratio was estimated by Gill as approximately 1/12 (or alternatively $Ra > 20000$). The temperature field, when plotted in a similar manner, also reflects the theory's success for large Ra (Fig. 11b).

a)

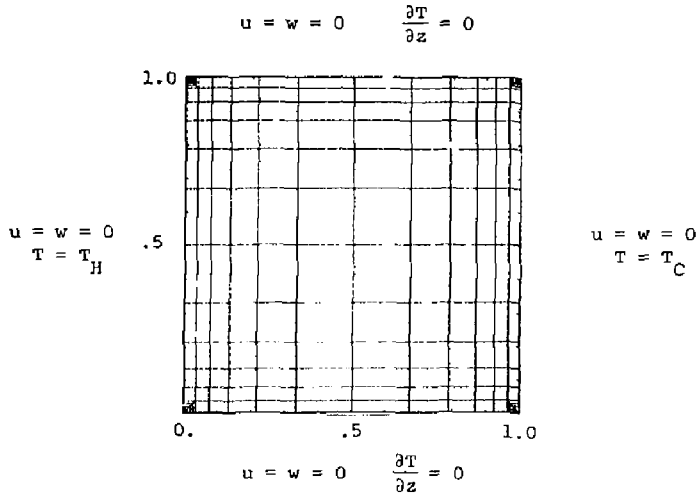

b)

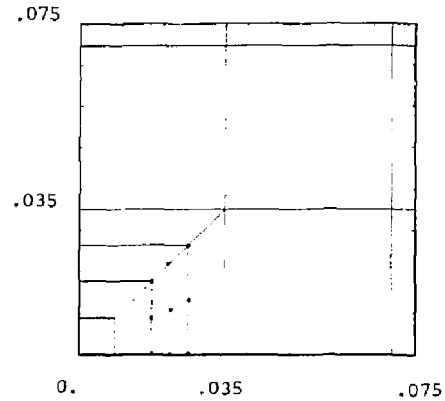

Figure 1 Computational grid.
a) Domain and boundary conditions.
b) Details of the mesh in a corner.

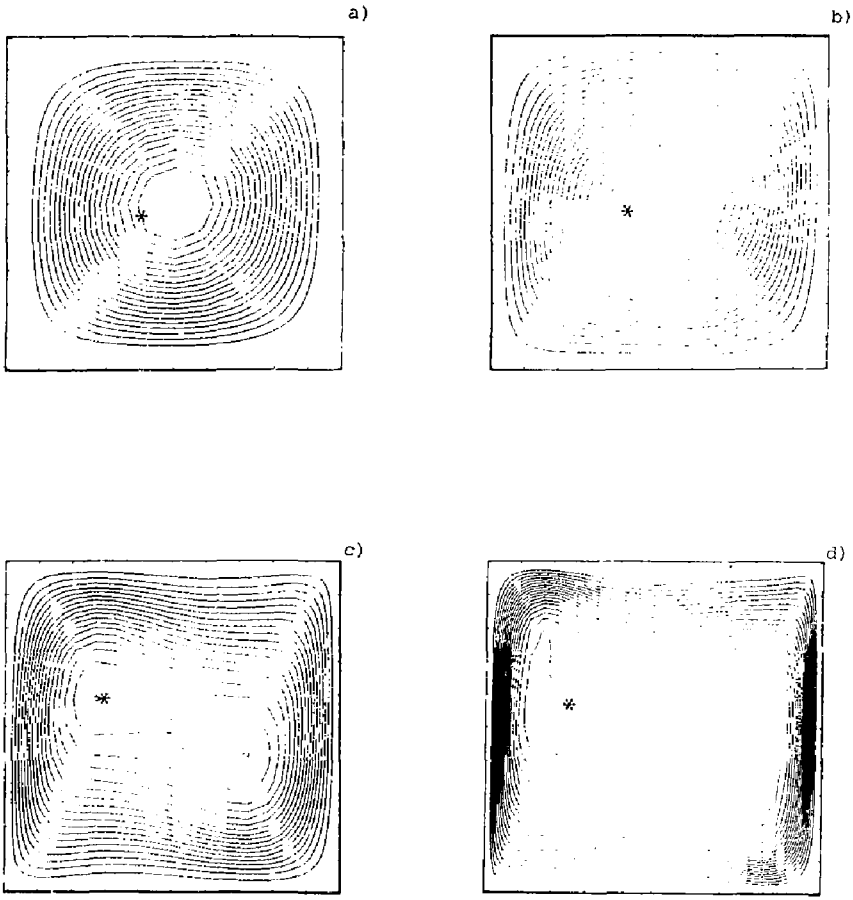

Figure 2 Stream function.

a)	$Ra = 10^3$	* = 1.07	$\Delta\psi$ = -.053
b)	$Ra = 10^4$	* = 4.84	$\Delta\psi$ = -.24
c)	$Ra = 10^5$	* = 10.7	$\Delta\psi$ = -.266
d)	$Ra = 10^6$	* = 18.5	$\Delta\psi$ = -.94

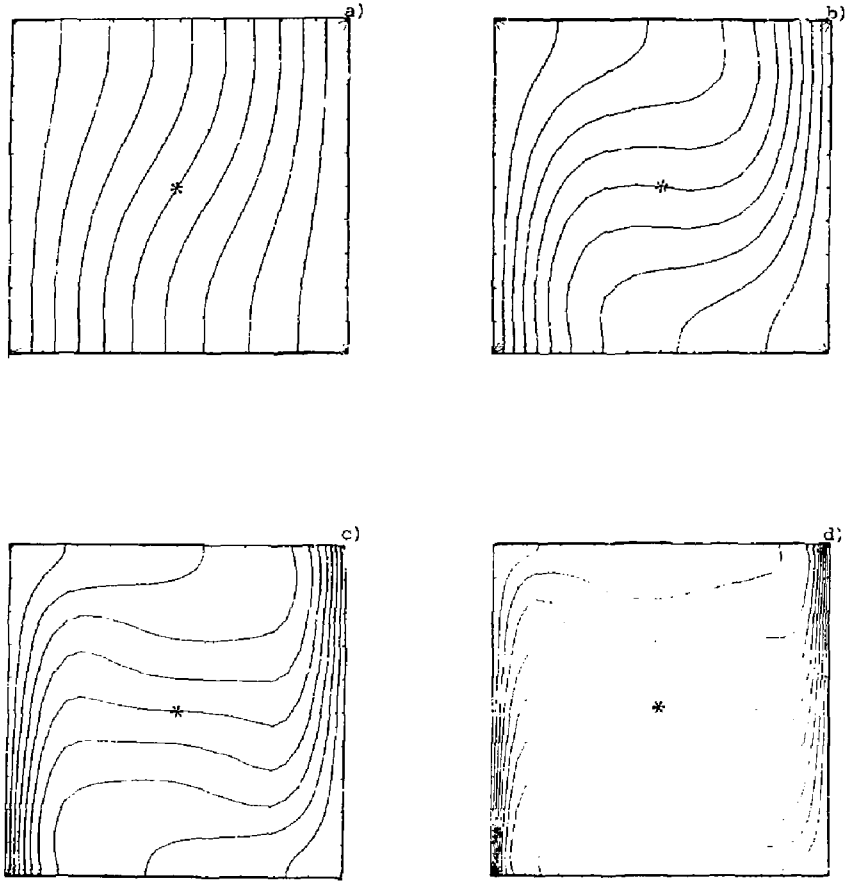

Figure 3 Temperature * = 0.0 $\Delta T = \pm .1$
a) Ra = 10^3
b) Ra = 10^4
c) Ra = 10^5
d) Ra = 10^6

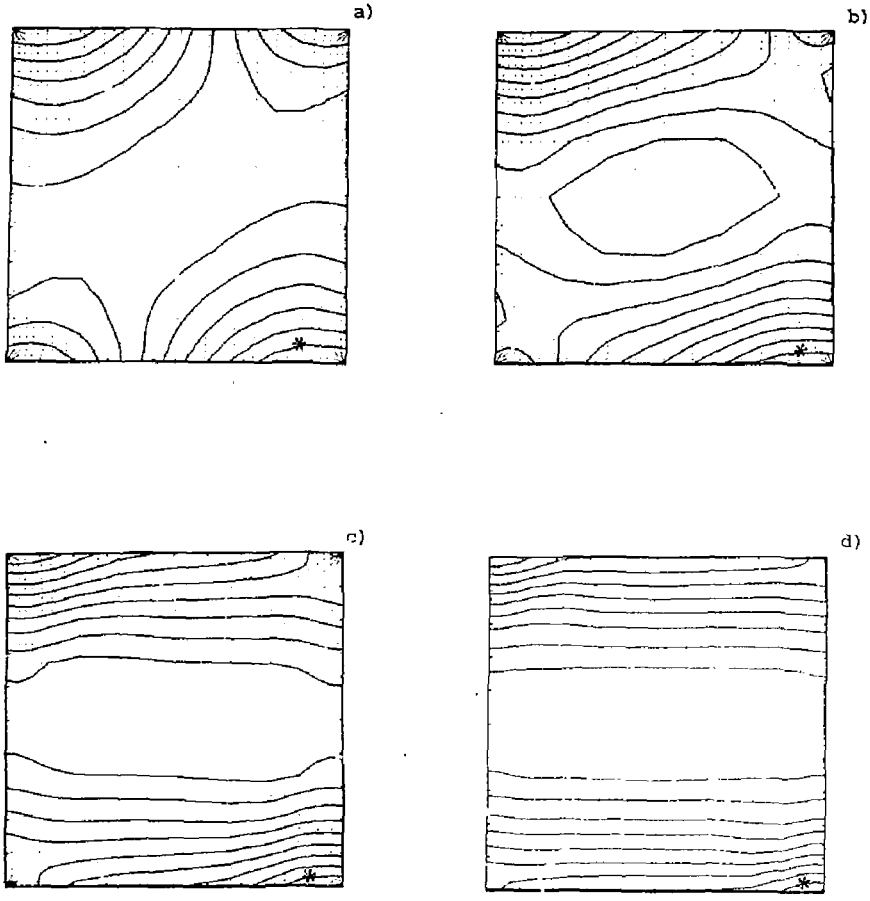

Figure 4 **Pressure**

a)	$Ra = 10^3$	$* = 79.14$	$\Delta P = -16.84$
b)	$Ra = 10^4$	$* = 7.659 \times 10^2$	$\Delta P = -1.255 \times 10^2$
c)	$Ra = 10^5$	$* = 6.315 \times 10^3$	$\Delta P = -1.002 \times 10^3$
d)	$Ra = 10^6$	$* = 5.452 \times 10^4$	$\Delta P = -8.932 \times 10^3$

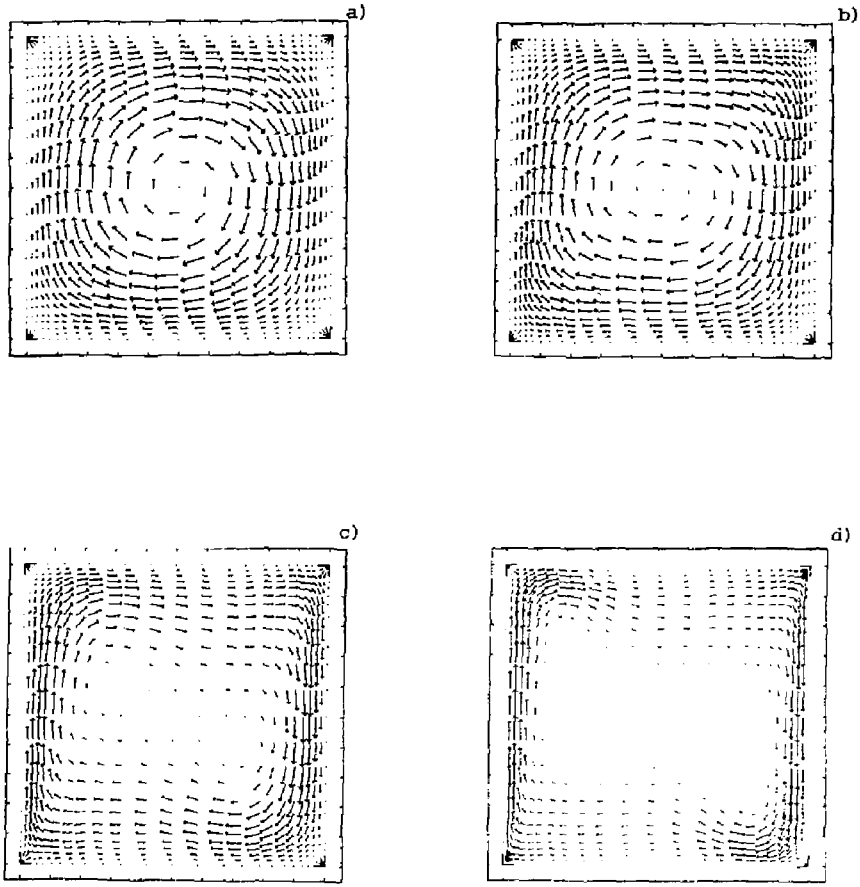

Figure 5 Velocity.

a) $Ra = 10^3$ $|\underline{u}|_{max} = 3.7$
b) $Ra = 10^4$ $|\underline{u}|_{max} = 19.7$
c) $Ra = 10^5$ $|\underline{u}|_{max} = 68.9$
d) $Ra = 10^6$ $|\underline{u}|_{max} = 220.6$

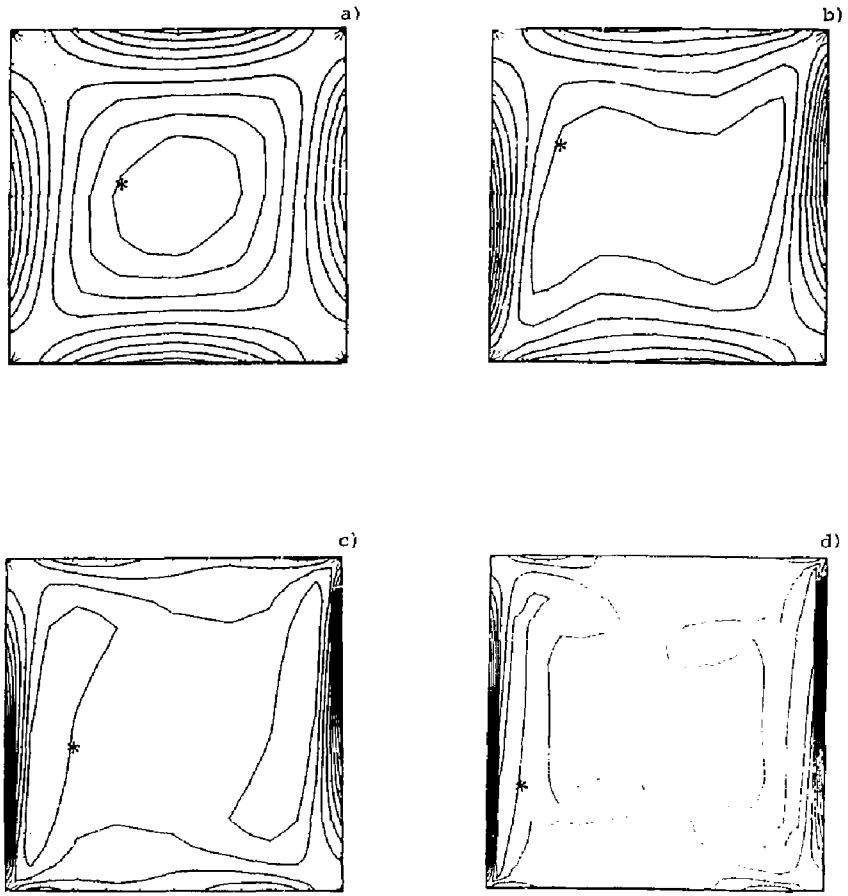

Figure 6 Vorticity (Ω).

a)	Ra = 10^3	* = -25.3	$\Delta\Omega$ = 8.47
b)	Ra = 10^4	* = -74.5	$\Delta\Omega$ = 54.9
c)	Ra = 10^5	* = -319.0	$\Delta\Omega$ = 333.0
d)	Ra = 10^6	* = -1800.0	$\Delta\Omega$ = 2050.0

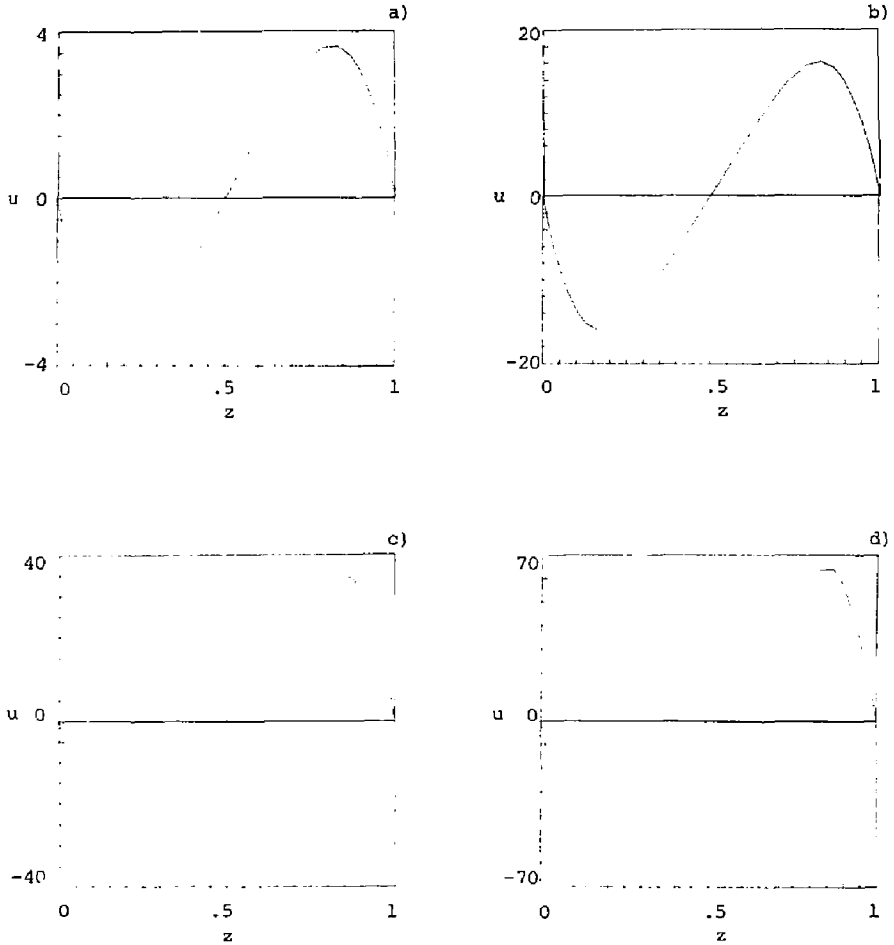

Figure 7 Horizontal velocity at x = .5
a) Ra = 10^3
b) Ra = 10^4
c) Ra = 10^5
d) Ra = 10^6

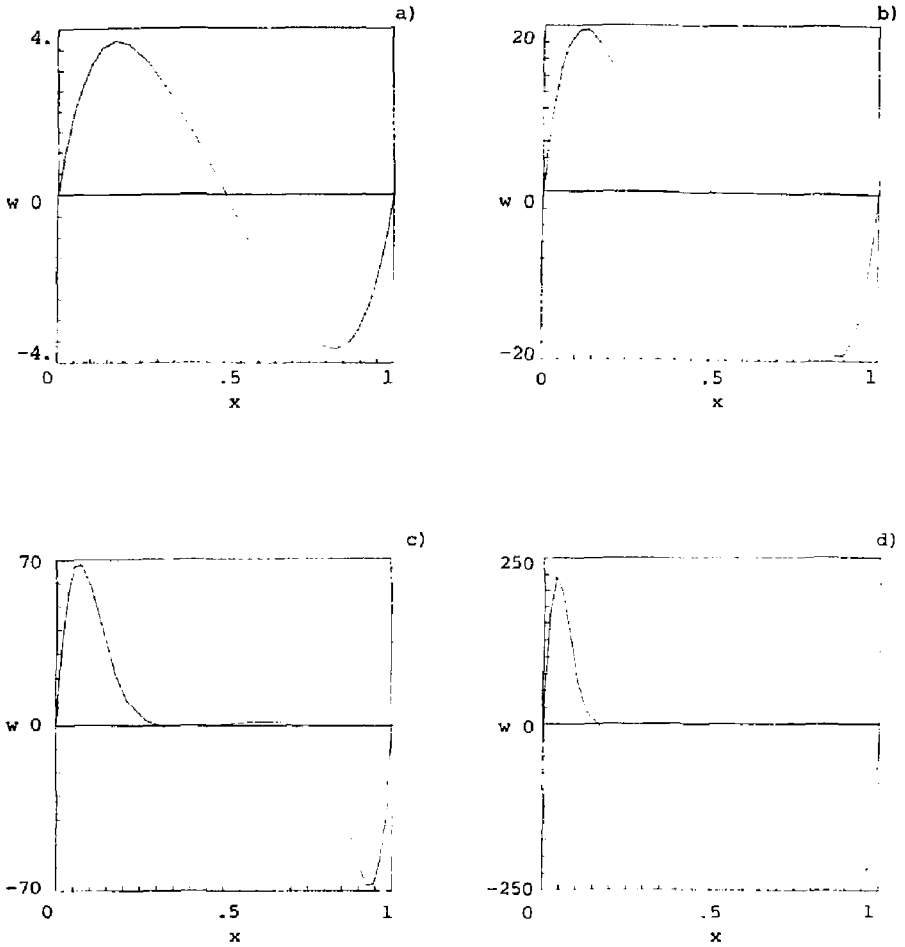

Figure 8 Vertical velocity at z = .5
a) Ra = 10^3
b) Ra = 10^4
c) Ra = 10^5
d) Ra = 10^6

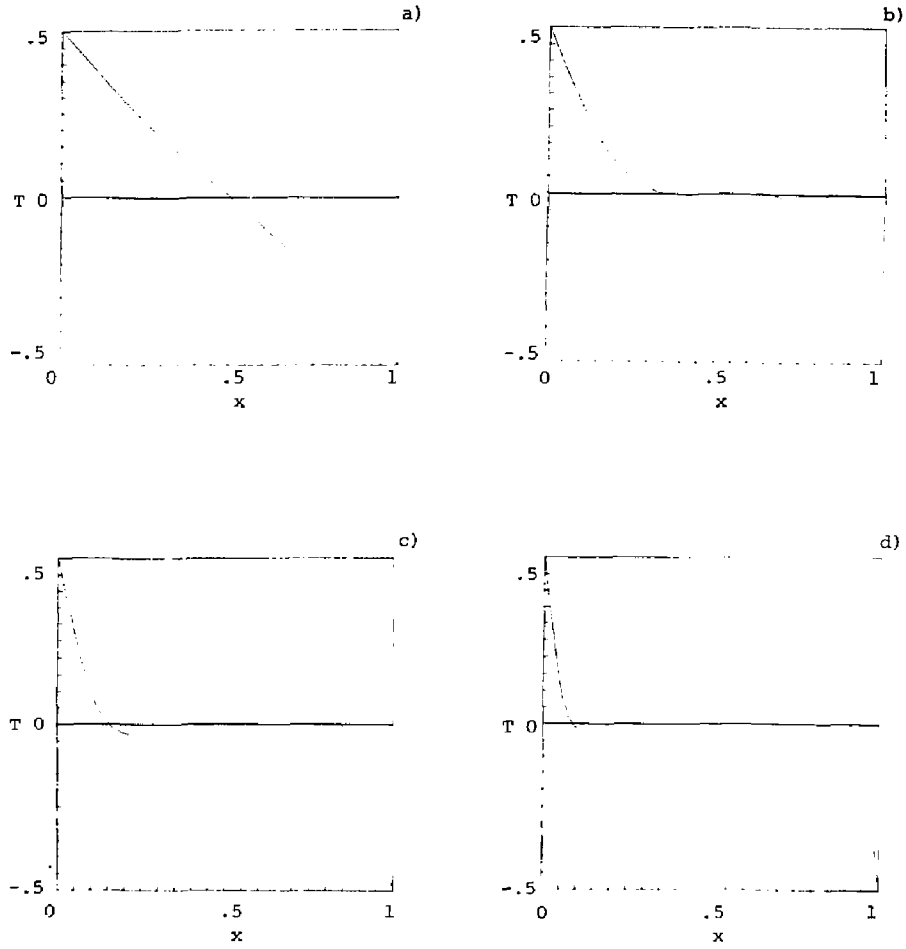

Figure 9 Temperature at z = .5
a) Ra = 10^3
b) Ra = 10^4
c) Ra = 10^5
d) Ra = 10^6

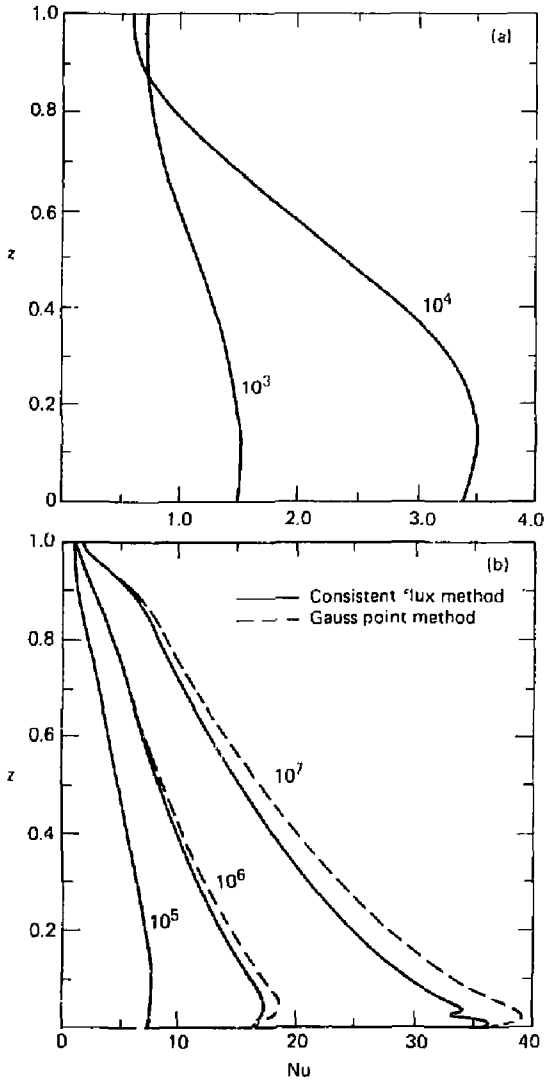

Figure 10 Heat flux at cold wall
a) Ra = 10^3, 10^4
b) Ra = 10^5, 10^6, 10^7

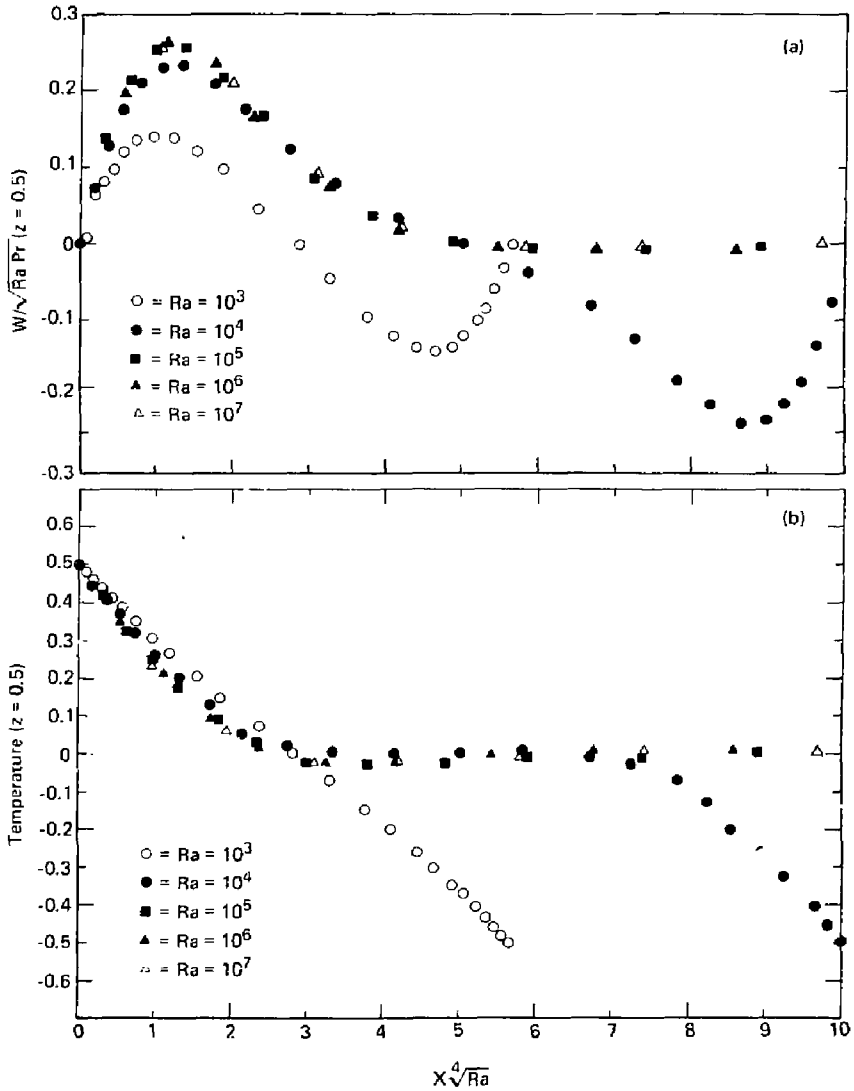

Figure 11 a) Scaled vertical velocity in boundary layer (z = .5).
b) Temperature in boundary layer (z = .5).

TABLE 2

Ra	W_{max} @ z=.5	U_{max} @ x=.5	Nu_{cf} (ave)	Nu_{cf} (max)	Nu_{cf} (min)	Nu_{gp} (ave)	Nu_{gp} (max)	Nu_{gp} (min)	ψ_{max}	Number of iterations
10^3	3.7040 @ x=.166	3.656 @ z=.812	1.1178	1.5065 @ z=.0746	.6912 @ z=1.0	1.1173	1.5064 @ z=.087	.6912 @ z=.998	1.1754 x=.5 z=.5	4
10^4	19.675 @ x=.1187	16.193 @ z=.822	2.2449	3.535 @ z=.1315	.5850 @ z=1.0	2.2479	3.5351 @ z=.15	.5852 @ z=.998	5.0753 x=.5 z=.5	4
10^5	68.896 @ x=.0663	34.620 @ z=.856	4.5211	7.731 @ z=.0746	.7277 @ z=1.0	4.5586	7.8099 @ z=.087	.728 @ z=.998	9.6206 x=.728 z=.416	4
10^6	220.64 @ x=.0316	64.593 @ z=.850	8.8170	17.294 @ z=.045	.9805 @ z=1.0	9.1699	18.508 @ z=.043	.9837 @ z=.998	16.707 x=.828 z=.5	6
10^7	728.23 @ x=.0237	147.56 @ z=.888	16.3400	36.503 @ z=.011	1.4158 @ z=1.0	18.1798	39.1829 @ .019	1.4302 @ z=.998	29.697 x=.897 z=.416	7*

*An intermediate step at Ra = 5 x 10^6 was needed for an initial guess.

Part 2

HIGHER RAYLEIGH NUMBER FLOW ($Ra = 10^7$) AND A FEW NEW TWISTS

Since no difficulty was encountered in solving the given problems, we pushed on a bit, partly to test the limits of our code, and partly to provide some ideas for more difficult and informative test problems.

A simulation at an elevated Rayleigh number was attempted with generally predictable results (the solution was more difficult to obtain - see Table 2). As stated previously the discretization near the wall is probably not fine enough for very accurate results in the boundary layer, however the overall agreement with previous solutions[3,7] is still quite good (Figs. 12 and 13).

The difference between the Gauss point method for calculating heat flux and the consistent method becomes apparent near $Ra = 10^6$, and has greatly intensified by $Ra = 10^7$ (Fig. 10b). This discrepancy has two possible explanations, the first being that the difference occurs in an area having a large horizontal thermal gradient accompanied by a mild outward convex bending of the isotherms (Figs. 14b,d). This vertical temperature gradient results in some heat transport in the z direction, a contribution to the Nusselt number that the Gauss point method doesn't account for and thereby calculates a larger magnitude. (Note the relatively large velocities in the lower left corner in Figs. 14a and 14c). At $Ra = 10^7$ the vertical gradient is more complicated yet and the flux minimum near $z = 0.0306$ reflects it (Fig. 10b). In general we believe that the more conventional Gauss point heat flux predictions are slightly too high. The second possible expanation is a combination of a

lack of adequate grid refinement coupled with a fairly abrupt change in element size near the corners. (Viewed in retrospect, our grid refinement in the corners could have been better).

Convection in an Inclined Cavity

A series of numerical experiments at Ra = 10^6 was made with the domain tilted at five different angles, θ, with respect to the vertical: (the direction of gravity) $\theta = \pm 30^\circ, \pm 60^\circ, -90^\circ$. The cavity in its normal orientation corresponds to $\theta = 0^\circ$, Bénard flow corresponds to $\theta = -90^\circ$, and the trivial no-flow, heated from above, condition is $\theta = +90^\circ$.

A substantial amount of work has been performed experimentally, theoretically, and numerically for a variety of different angles and aspect ratios.[8,9,10] The majority of the literature available however is devoted to lower Rayleigh numbers or aspect ratios substantially different than unity, which is investigated here.

Large changes occur in the flow field once the cavity has been rotated slightly. For small negative tilts (at Ra = 10^6) the flow enters a transitional region where the two dimensional assumption is apparently no longer valid. Hart[8] studied this regime (for low aspect ratios) and concluded that there are few truly two-dimensional solutions at any tilt - positive or negative, at this Rayleigh number. When rotated, the unicellular, transverse flow at $\theta = 0^\circ$ gives way to instabilities which are usually in the form of longitudinal roll cells centered at z = .5 and periodic in the y-direction. The net result is a complex, three-dimensional flow field. At tilt angles less than

approximately -20°, Hart predicts a turbulent flow and at positive angles (again near 20°) a laminar characteristic is present, which again undergoes a transformation before reaching convective stability at $\theta = 90^{\circ}$. While the conditions investigated by Hart (a small aspect ratio) are substantially different than those studied in this report, it seems safe to assume that the results presented here for $\theta < -30^{\circ}$ probably have little physical significance. Solutions at tilt angles of large magnitude are included here only for insight into the two dimensional simplification of this complex and perhaps unstable three dimensional flow.

Each tilted cavity simulation (except $\theta = -90^{\circ}$) used a simpler solution (smaller angle of tilt) as an initial guess. Since we were unable to obtain solutions (divergent iterations) beyond $\theta = -67^{\circ}$, the "Bénard" result was obtained by working up from $Ra = 10^4$, 10^5, and finally to $Ra = 10^6$ (thus possibly reflecting the complex behavior near $\theta = -70^{\circ}$ to -90° indicated by Arnold et al.[9]).

The solution at $\theta = -30^{\circ}$ (Fig. 15; see also Table 3) clearly shows major changes from its $\theta = 0^{\circ}$ counterpart. The overall flow strength has increased, and the maximum velocity is now located just off the insulated wall. The central core is becoming isothermal (no longer stably stratified) and the thermal boundary layer less steep as is reflected in the reduced Nusselt number (Table 3). Large perturbations in the pressure solution from the hydrostatic distribution can be seen near the walls, particularly at the left and right hand corners where velocities are quite large.

Tilting the cavity to -60° (Fig. 16) results in a continuation of the flow pattern established at $\theta = -30^{\circ}$, with the exceptions of the

unicellular characteristic and an essentially isothermal core. Overall flow strength has increased and the Nusselt number decreased. The velocity field is approaching overall symmetry as is reflected in the stream function.

The velocity field of the enclosed Bénard solution at $\theta = -90^{\circ}$ (Fig. 17) qualitatively resembles the $\theta = 0^{\circ}$, $Ra = 10^3$ solution. Closer investigation, however, reveals a more vigorous flow with recirculation eddies in all corners (Fig. 17e). These recirculations, while quite feeble (the larger two being roughly 30 times weaker than the base flow), have a substantial effect on the heat transfer, forcing the maximum Nusselt number to migrate towards the midside and drop markedly in magnitude.

Rotating the cavity in the opposite direction to $\theta = +30^{\circ}$ (Fig. 18) causes the vortex center to separate and migrate towards the horizontally oriented corners. The circulation strength decreases from its maximum at $\theta = 0^{\circ}$ and the most active corners are the "horizontal" ones (as is true in all the tilted cavity results). The heat flux has dropped to a value that agrees quite well with Catton et al.[10] As in the $\theta = 0^{\circ}$ simulation, the pressure field is largely hydrostatic.

Although the stream function indicates complex motion for the $\theta = 60^{\circ}$ result (Fig. 19), the magnitude of overall flow is substantially weaker. The Nusselt number again correlates with that in the literature.[10]

Basic flow characteristics for the above five tilted cavity simulations are contained in Table 3.

Conclusions

The solution for the given comparison problems were easily obtained and the results show good agreement with prior work. A new technique for heat flux calculation was reported with results, however, that differ with others at large Ra. This new method, which can also guarantee a global heat balance, is probably superior to the traditional method.

Additional problems were investigated in the second section of this paper in order to test our computer program's performance and to suggest new, more difficult comparison problems. A final suggestion for a challenging test simulation is that of thermal convection in a vertical slot, with an aspect ratio of 5 or 10 (or perhaps 20), in which very complex flow fields are known to exist (see Elder[11] and De Vahl Davis[12]), with multiple secondary, and even tertiary cells. We have experience in this area (an aspect ratio of 20 and Pr = 1000) and can attest to its difficulty.

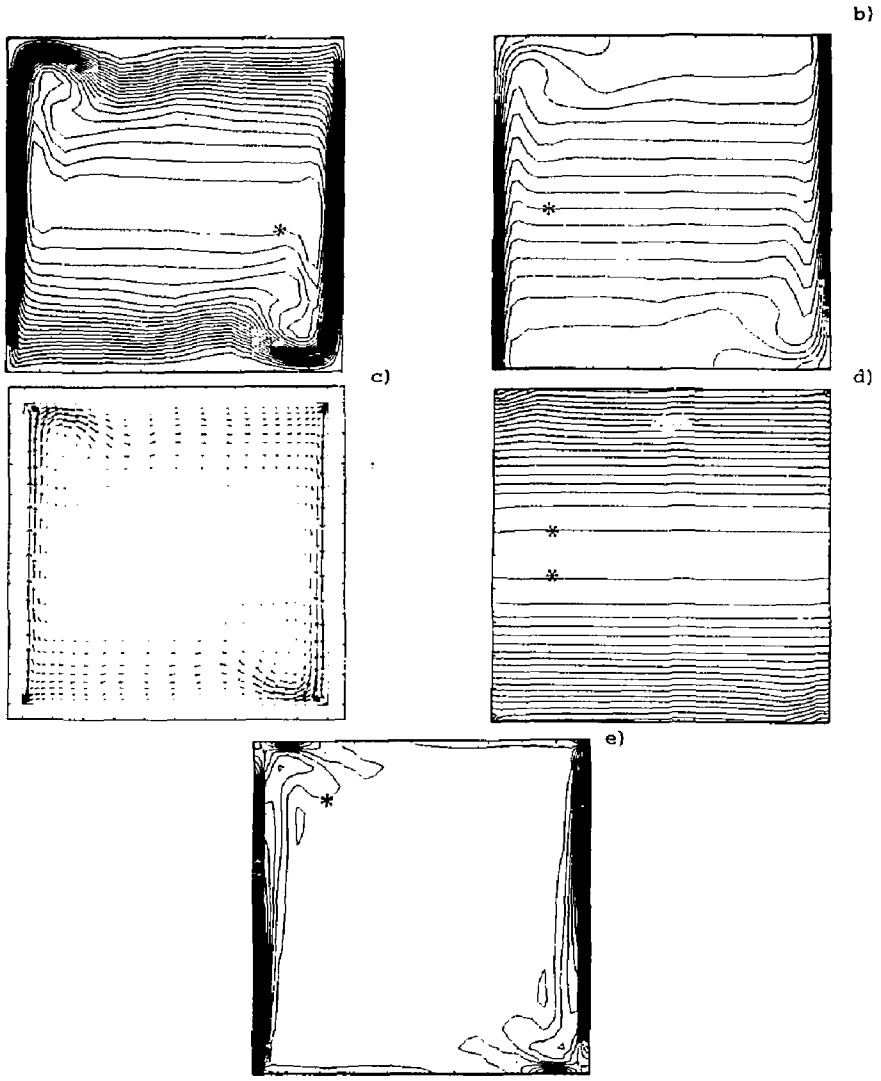

Figure 12 Simulation at Ra = 10^7.

a)	Stream function (ψ)	* = 26.6	$\Delta\psi$ = −1.6
b)	Temperature (T)	* = −0.024	$\Delta T = \pm .047$
c)	Velocity (u)	$\lvert\underline{u}\rvert_{max}$ = 687.4	
d)	Pressure (P)	* = -2.25×10^6	$\Delta P = 4.02 \times 10^5$
e)	Vorticity (Ω)	* = -1.98×10^3	$\Delta\Omega = 4.42 \times 10^3$

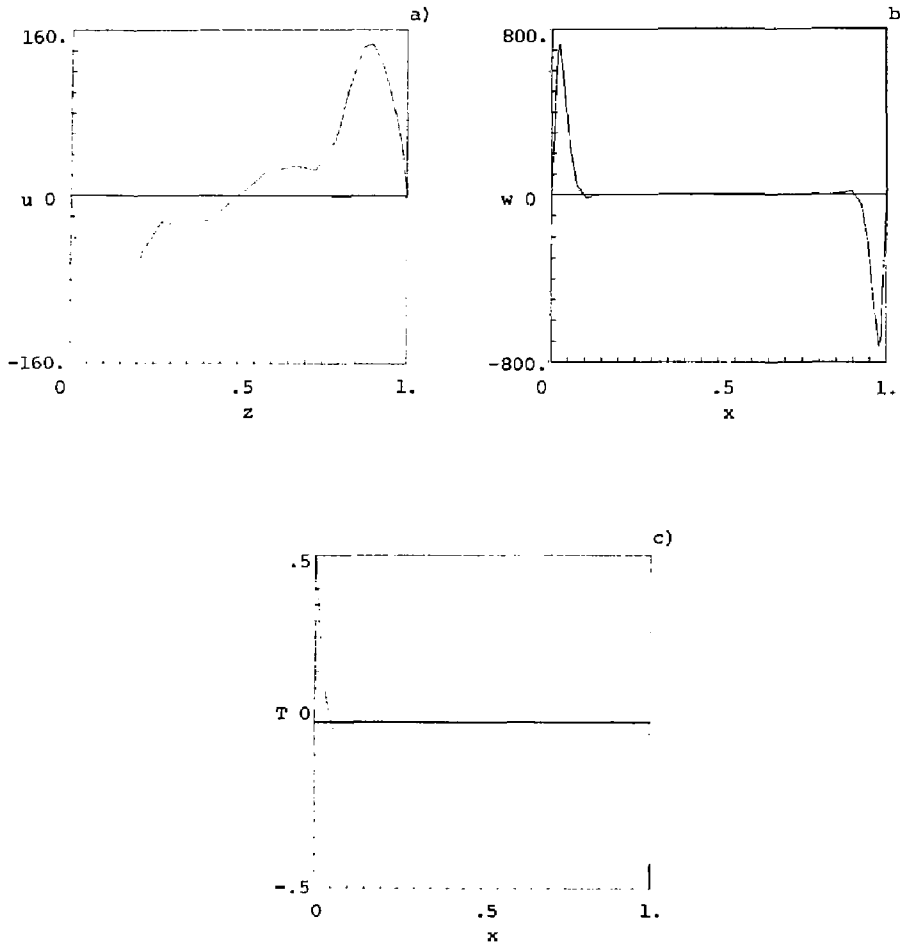

Figure 13 Midcavity profiles for Ra = 10^7.
a) Horizontal velocity at x = .5
b) Vertical velocity at z = .5
c) Temperature at z = .5

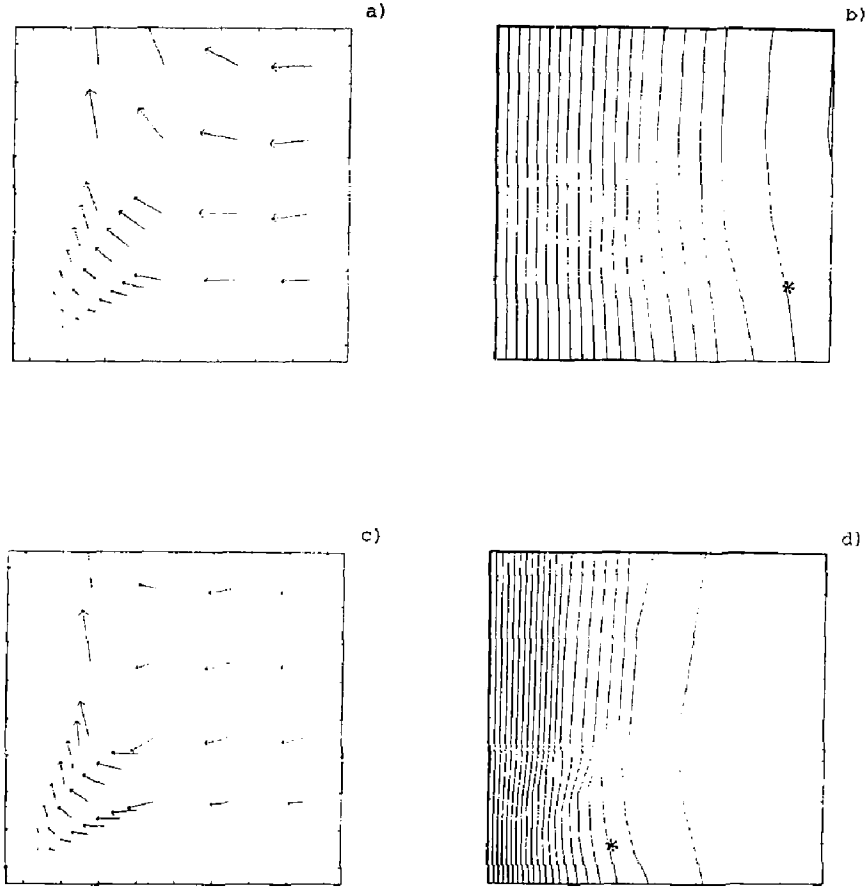

Figure 14 Details of lower lefthand corner: velocity and temperature.
a) $Ra = 10^6$ $|u|_{max} = 85,5$
b) $Ra = 10^6$ * = -.22 ΔT = .04
c) $Ra = 10^7$ $|u|_{max} = 313.0$
d) $Ra = 10^7$ * = -.22 ΔT = .04

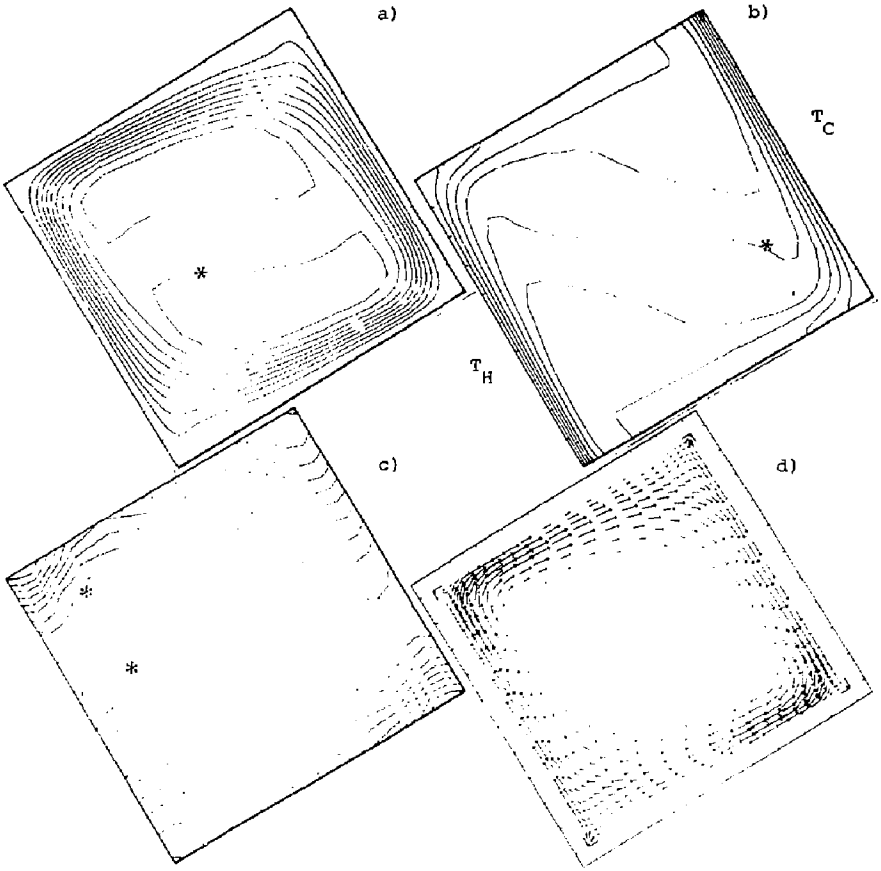

Figure 15 $\theta = -30^{o}$, heated from below, $Ra = 10^{6}$.

a)	Stream function	* = 24.4	$\Delta\psi = 2.74$
b)	Temperature	* = 0.	$\Delta T = \pm.1$
c)	Pressure	* = -1.23×10^{5}	$\Delta P = 6.500 \times 10^{4}$
d)	Velocity	$\lvert \underline{u} \rvert_{max} = 267.$	

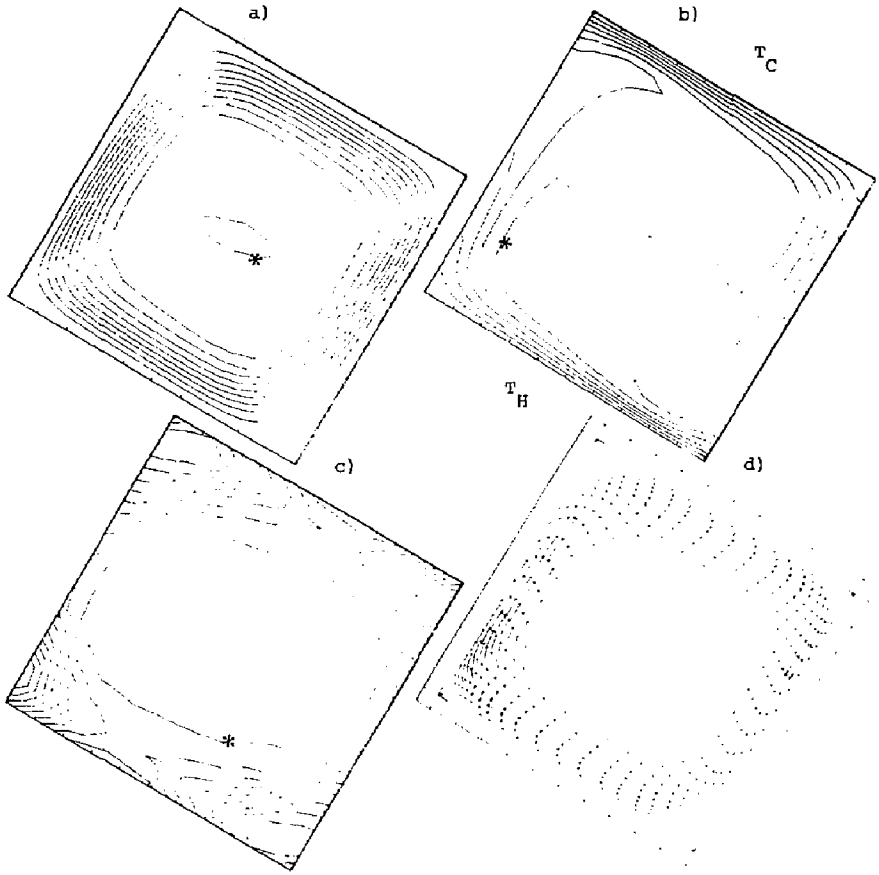

Figure 16 $\theta = -60^{o}$, heated from below, $Ra = 10^{6}$.

a)	Stream function	* = 35.6	$\Delta\psi = 3.92$
b)	Temperature	* = 0.0	$\Delta T = \pm.1$
c)	Pressure	* = -6.76×10^{4}	$\Delta p = 5.23 \times 10^{4}$
d)	Velocity	$\lvert \underline{u} \rvert_{max} = 338.$	

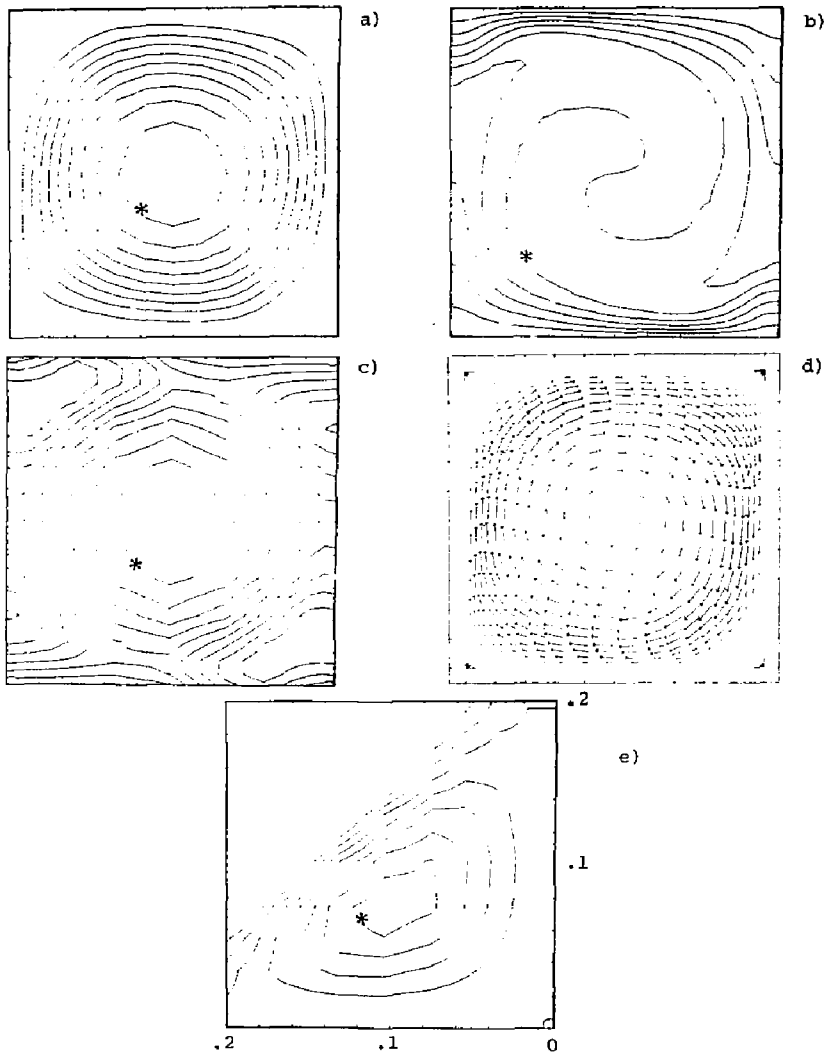

Figure 17 "Bénard" flow, heated from below, $\theta = -90$, $Ra = 10^6$.

a)	Stream function	* = 73.5	$\Delta\psi$ = 8.34
b)	Temperature	* = 0.0	$\Delta T = \pm .1$
c)	Pressure	* = -1.46×10^5	$\Delta P = 3.89 \times 10^4$
d)	Velocity	$\lvert \underline{u} \rvert_{max} = 339.$	
e)	Close-up of a corner recirculation	* = -2.35	$\Delta\psi$ = .337

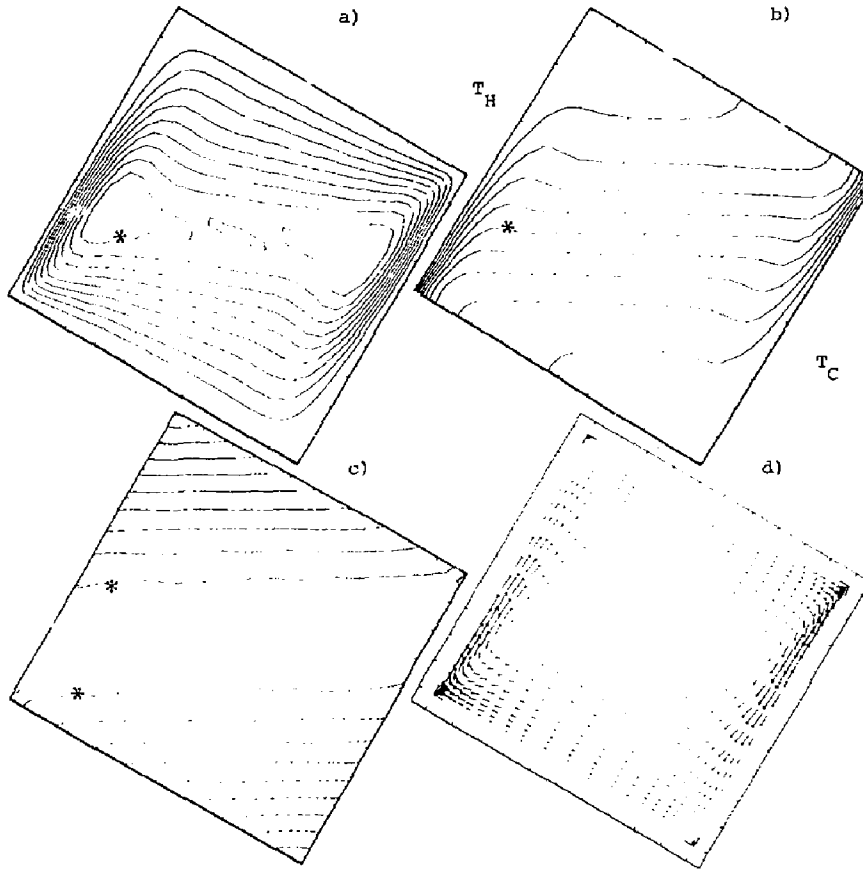

Figure 18 $\theta = +30^{\circ}$, heated from above, Ra = 10^6.

a)	Stream function	* = 7.93	$\Delta\psi$ = .869
b)	Temperature	* = 0.0	$\Delta T = \pm .1$
c)	Pressure	* = -2.17×10^5	$\Delta P = 1.69 \times 10^5$
d)	Velocity	$\lvert \underline{u} \rvert_{max} = 129.$	

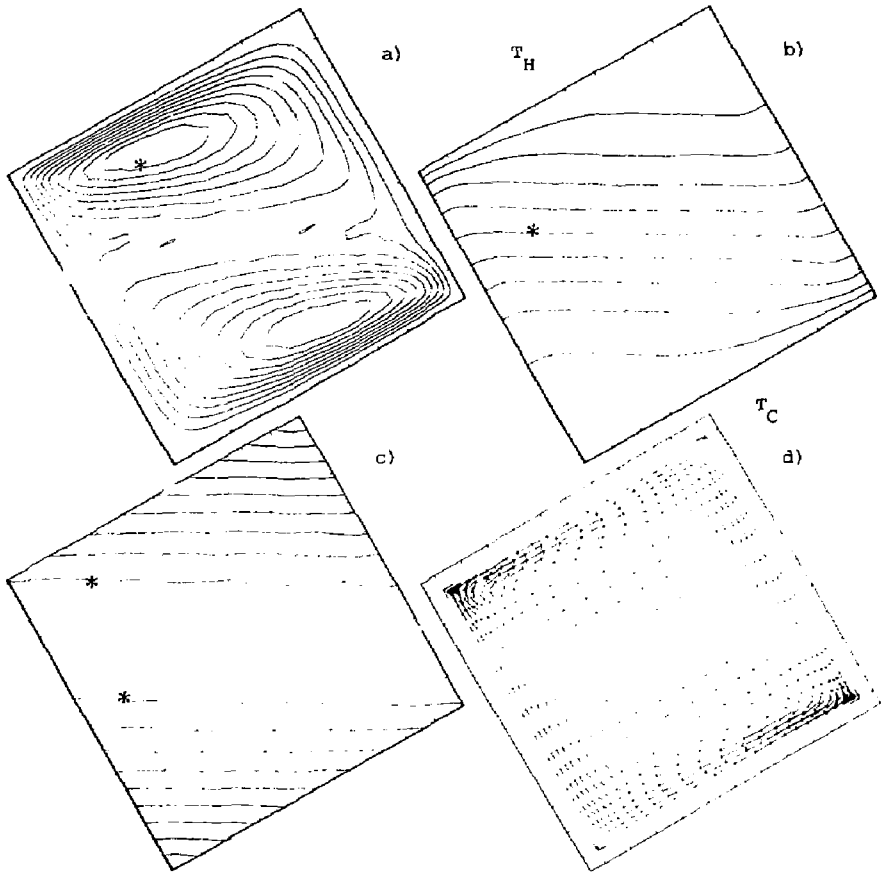

Figure 19 $\theta = +60^{\circ}$, heated from above, $Ra = 10^6$.

a)	Stream function	* = 2.7	$\Delta\psi$ = .307
b)	Temperature	* = 0.0	$\Delta T = \pm .1$
c)	Pressure	* = -1.97×10^5	$\Delta P = \pm 1.64 \times 10^5$
d)	Velocity	$\lvert \underline{u} \rvert_{max} = 36.1$	

TABLE 3

θ	Maximum Velocity	$Nu(ave)_{cf}$	$Nu(max)_{cf}$	$Nu(min)_{cf}$	ψ_{max}	$\psi(.5,.5)$	P_{max}	Number of iterations from previous solution
-90^{o}	338.65 @ (.5,.0746)	5.008	8.616 @ z=.331	1.184 @ z=1.0	81.800 @ (.5,.5)	81.8	2.051×10^{4} @ (.031,.035)	14*
-60^{o}	337.63 @ (.585,.055)	7.893	12.38 @ z=.213	1.447 @ z=1.0	39.633 @ (.272,.416)	35.12	4.019×10^{4} @ (.031,.0)	5
-30^{o}	266.52 @ (.727,.055)	8.711	13.09 @ z=.046	1.507 @ z=1.0	27.033 @ (.415,.272)	23.33	4.575×10^{4} @ (.031,0.)	7
0^{o}	220.64 @ (.032,.5)	8.817	17.29 @ z=.045	.9805 @ z=1.0	16.707 @ (.828,.5)	16.37	6.353×10^{4} @ (.031,0)	6
30^{0}	128.58 @ (.035,.272)	5.316	15.70 @ z=.035	.2034 @ z=1.0	8.810 @ (.868,.585)	8.057	1.294×10^{5} @ (.031,0)	7
60^{o}	36.14 @ (.035,.272)	1.566	4.492 @ z=.026	.2155 @ z=1.0	2.991 @ (.868,.585)	.6246	1.280×10^{5} @ (.031,0)	4

*This solution followed from $\theta = -90^{o}$ at $Ra = 10^{4}$ (5 iter.), $Ra = 10^{5}$ (5 iter.) and $Ra = 10^{6}$ (4 iter.).

References

1 G. de Vahl Davis, I. P. Jones, P. J. Roache, Computers and Fluids, 7, 315-316 (1979).

2. G. D. Mallinson, G. de Vahl Davis, "Three-Dimensional Natural Convection in a Box: A Numerical Study", J. Fluid Mech. 83, 1-31 (1977).

3. R. S. Marshall, J. C. Heinrich, O. C. Zienkiewicz, "Natural Convection in a Square Enclosure by a Finite Element, Penalty Function Method using Primitive Fluid Variables", Num. Heat Transfer 1, 315-330 (1978).

4. Hood, P., "Frontal Solution Method for Unsymmetric Matrices," Int. J. for Num. Meth. Eng., 10, 379-399, (1976).

5. P. M. Gresho and R. L. Lee, in preparation.

6. R. L. Lee, P. M. Gresho, R. L. Sani, "Smoothing Techniques for Certain Primitive Variable Solutions of the Navier-Stokes Equations", Int. J. Num. Meth. Eng., 14, 1785-1804 (1979).

7. A. E. Gill, "The Boundary-Layer Regime for Convection in a Rectangular Cavity", J. Fluid Mech. 26, 515-536 (1966).

8. J. E. Hart, "Stability of the Flow in a Differentially Heated Inclined Box", J. Fluid Mech. 47, 547-576 (1971).

9. J. N. Arnold, I. Catton, D. K. Edwards, "Experimental Investigation of Natural Convection in Inclined Rectangular Regions of Differing Aspect Ratios", Int. J. Heat Transfer, Trans. ASME, 67-71 Feb. (1976).

10. I. Catton, P. S. Ayyaswamy, R. M. Clever, "Natural Convection Flow in a Finite, Rectangular Slot Arbitrarily Oriented with Respect to the Gravity Vector", Int. J. Heat Mass Transfer 17, 173-184 (1974).

11. J. W. Elder, "Laminar Free Convection in a Vertical Slot," J. Fluid Mech., 23, 77-98 (1965).

12. G. de Vahl Davis, G. D. Mallinson, "A Note on Natural Convection in a Vertical SLot," J. Fluid Mech., 72, 87-93 (1975).